

The Structure of the Cobalt Oxide/Au Catalyst Interface in Electrochemical Water Splitting

Jakob Fester, Anton Makoveev, Doris Grumelli, Rico Gutzler, Zhaozong Sun, Jonathan Rodríguez-Fernández, Klaus Kern, and Jeppe V. Lauritsen*

Abstract: The catalytic synergy between cobalt oxide and gold leads to strong promotion of the oxygen evolution reaction (OER)—one half-reaction of electrochemical water splitting. However, the mechanism behind the enhancement effect is still not understood, in part due to a missing structural model of the active interface. Using a novel interplay of cyclic voltammetry (CV) for electrochemistry integrated with scanning tunneling microscopy (STM) and X-ray photoelectron spectroscopy (XPS) on an atomically defined cobalt oxide/Au(111) system, we reveal here that the supporting gold substrate uniquely favors a flexible cobalt-oxyhydroxide/Au interface in the electrochemically active potential window and thus suppresses the formation of less active bulk cobalt oxide morphologies. The findings substantiate why optimum catalytic synergy is obtained for oxide coverages on gold close to or below one monolayer, and provide the first morphological description of the active phase during electrocatalysis.

Hydrogen production via electrochemical or solar water splitting ($2\text{H}_2\text{O} \rightarrow \text{O}_2 + 2\text{H}_2$) is an advancing technology with the potential of providing an almost unlimited source of sustainable energy. Although promising, the realization potential of a large-scale production technology is currently limited by the slow kinetics of the oxygen evolution reaction (OER), which relies on expensive and scarce noble metal catalysts (Pt, Rh, Ir).^[1] However, cobalt oxides (among other abundant 3d-transition metal oxides, such as Ni, Fe) show great promise for the OER process in alkaline solution.^[2]

Optimization to meet requirements of stability, durability, and activity as well as lowering the applied overpotential during OER operation is ongoing. These approaches include catalyst nanostructuring^[2d,3] or the use of mixed oxides.^[4] In addition, synergistic effects of oxides in combination with gold and other noble metals^[5] are attracting strong attention in novel electrocatalysts.^[6] To support such concepts, much effort has focused on the reaction mechanisms and active species in cobalt oxide OER catalysts through theoretical modeling^[7] and in situ spectroscopic techniques.^[8] Importantly, the cobalt oxide system is structurally and compositionally very dynamic as it may pass through several potential and pH-value induced transformations from its initial phase, that is, from inactive spinel Co_3O_4 or CoO into $\text{CoO}(\text{OH})$ oxyhydroxide and $\text{Co}(\text{OH})_2$ hydroxide.^[7d,9] There appears to be consensus that Co^{4+} active centers are present under OER,^[5a,7c,8b] and the activity is usually attributed to the $\text{CoO}(\text{OH})$ -like oxyhydroxide as the main active phase.^[9a,10] The exact nature and location of the active sites and reaction mechanisms occurring on this active phase is, however, still debated.^[11]

Here, taking advantage of an experimental setup for transfer of an atomically well-characterized sample back and forth between an ultra-high vacuum scanning tunneling microscope (STM) and an electrochemical cell,^[12] we provide direct structural insight into the transformations of the cobalt oxide/Au interface in the potential window relevant for electrochemical water splitting and relate these to the measured catalytic activity. To elucidate the catalytic cobalt oxide/Au interface at atomic resolution by means of STM and X-ray photoelectron spectroscopy (XPS) we recently established a model system for cobalt oxide on an Au(111) single crystal.^[13] An STM image illustrating the morphology of the atomically defined Co oxide/Au(111) system in its pristine state prior to electrochemistry experiments is shown in Figure 1a. The vacuum-synthesized (see experimental section) cobalt oxide nanoislands adopt a well-defined hexagonal shape that exposes both potentially active edge and basal plane sites. In this initial low-oxidized state of Co, the island structure reflects a strained Co–O bilayer (Figure 1b) with an overall stoichiometry between cobalt and oxygen close to one.^[13] Atom-resolved STM images of the top facet (basal plane) (inset in Figure 1a) reveal an overall unperturbed and clean hexagonal atomic lattice free of adsorbates in the pristine state, and with a characteristic ≈ 37 Å moiré pattern (large rhombic unit cell) that arises due to the 13.9% lattice mismatch of the Co–O bilayer with the underlying Au(111).

The electrocatalytic activity of the freshly prepared Co–O model catalyst towards HER and OER was explored by cyclic

[*] J. Fester, Z. Sun, J. Rodríguez-Fernández, J. V. Lauritsen
Interdisciplinary Nanoscience Center (iNANO), Aarhus University
8000 Aarhus C (Denmark)
E-mail: jvang@inano.au.dk

A. Makoveev
CEITEC BUT, Brno University of Technology
Purkynova 123, 621 00 Brno (Czech Republic)

D. Grumelli
Instituto de Investigaciones Fisicoquímicas Teóricas y Aplicadas
(INIFTA), Facultad de Ciencias Exactas, Universidad Nacional de La
Plata—CONICET
1900 La Plata (Argentina)

R. Gutzler, K. Kern
Max Planck Institute for Solid State Research
70569 Stuttgart (Germany)

K. Kern
Institute de Physique, Ecole Polytechnique Fédérale de Lausanne
1015 Lausanne (Switzerland)

Supporting information and the ORCID identification number(s) for the author(s) of this article can be found under:
<https://doi.org/10.1002/anie.201804417>

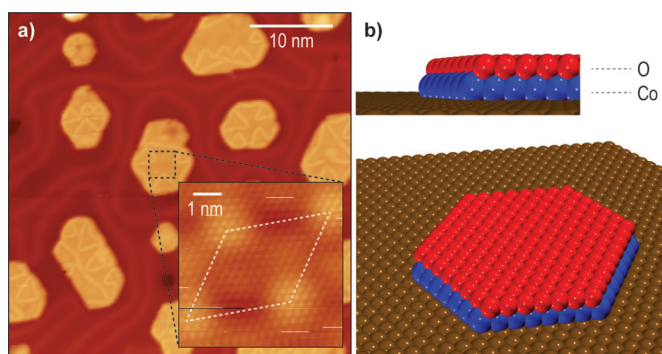


Figure 1. Co–O bilayer nanoislands on Au(111) in STM (a) and structural model (b). The inset in (a) shows a high-resolution image of the upper basal plane O atoms and the moiré pattern. Red spheres: O, blue spheres: Co. STM parameters: $-0.46\text{ V}/-0.16\text{ nA}$.

voltammetry (CV) in alkaline electrolyte (0.1 M NaOH) by transferring the sample into the electrochemical cell without exposing it to the ambient (see experimental section). Figure 2a graphs the cathodic branch (HER) for the freshly prepared bilayer (purple trace) and the bare Au(111) (grey trace) for comparison (see Figure SI.2 in the Supporting Information for all 10 scans). Whereas the Au(111) surface is inactive, the oxide covered sample exhibits an increase in current density with an onset below around -1.0 V vs. Ag/AgCl associated with HER. This onset value is comparable to

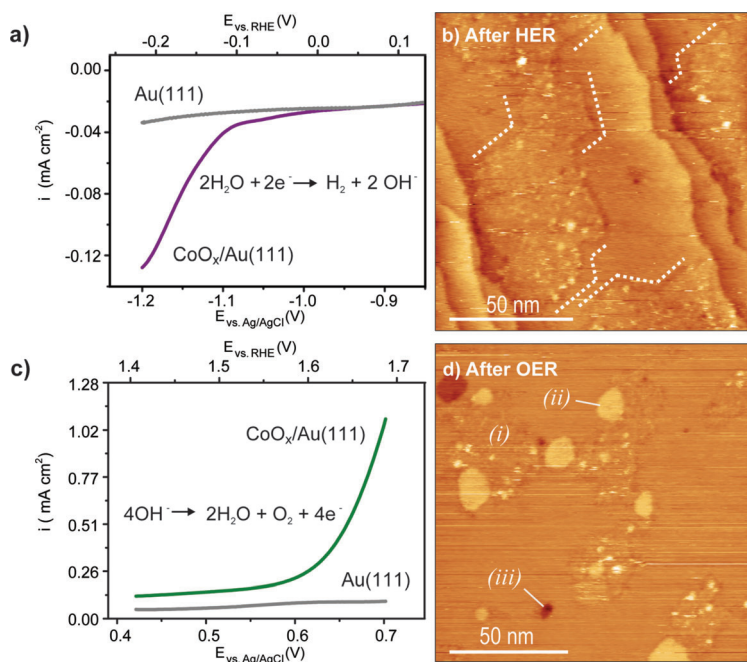


Figure 2. Cyclic voltammograms in the HER and OER potential regions and STM images of the surfaces after electrochemistry. a) Cathodic scan in the HER potential region for 0.3 ML Co–O/Au(111) (purple) compared to clean Au(111) (grey) in 0.1 M NaOH Ar saturated solution. Scan rate 0.05 Vs^{-1} . b) STM image of the cobalt oxide/Au(111) surface after HER corresponding to the cyclic voltammogram in (a). c) Anodic scan in the OER region for 0.3 ML Co–O/Au(111) (green) and clean Au(111) (grey) in 0.1 M NaOH Ar saturated solution. Scan rate 0.05 Vs^{-1} . d) The Co–O/Au(111) surface after OER. Italic numbers indicate cobalt oxide (i), gold islands (ii) and single atom deep pits in the Au(111) surface (iii). STM parameters: b) $1.56\text{ V}/0.20\text{ nA}$ and d) $0.95\text{ V}/0.41\text{ nA}$.

that already reported for Co oxides.^[14] Assuming 100% faradaic efficiency, the calculated TOF for hydrogen evolution at -1.2 V , corresponding to an overpotential of 0.22 V , is 2.4 electrons per second per cobalt atom.

The STM image in Figure 2b recorded after ten CV cycles at negative potentials reveals that the Co oxide amount (30% coverage) is stable on the surface, but the initial well-defined Co–O morphology has undergone reordering, reflecting significant agglomeration of the oxide material. A height measurement of $\approx 1.9\text{ \AA}$ (Figure SI.3) shows that the Co oxide is dispersed as an atomically thin layer, but instead of well-defined hexagonal nanoislands with a size of 10–30 nm (see also Figure SI.4), much larger (100 nm or more) patches now predominate. STM images at high magnification (Figure 2b) bear evidence of the cobalt oxide patches orientating themselves relative to the substrate. The island edge segments (white dotted lines) are in general straight and proceed along three distinguishable preferred directions that are oriented 120° relative to each other, implying that a crystalline, hexagonal island morphology terminated by low-index edges still predominates after CV. The STM images confirm a uniform flat structure only disturbed by a low density of bright dot-like protrusions that are likely to be small amounts of electrolyte deposits. To directly rule out a strong effect of electrodeposited compounds contributing to the observed phases, we analyzed a sample with a coverage gradient (4% to 44%) and found an oxide coverage consistent with the expected value everywhere along this gradient. It was not possible to reveal an atom-resolved ordered structural motif on the oxide from STM images, but the uniform height and clear absence of the moiré pattern specific to Co–O (Figure 1a, inset) strongly suggests a transformation into a different monolayer Co oxide structure consistent with epitaxial O–Co–O/Au(111).^[15]

Starting over with a freshly prepared Co–O bilayer sample with a coverage of 0.29 ML, Figure 2c graphs the CV curves for the OER anodic branch for Co oxide/Au (green trace) and bare Au(111) (grey trace) for comparison (see also Figure SI.5 and related description for the complete cyclic voltammogram). The as-prepared bilayer sample displays a high activity for OER indicated by a large increase in the current density with an onset around 0.55 V vs. Ag/AgCl, which translates to an overpotential of 0.30 V . The TOF for oxygen evolution at 0.60 V vs. Ag/AgCl corresponding to an overpotential of 0.35 V , is 2.6 electrons per second per cobalt atom, assuming a faradaic efficiency of 100%. In comparison, this TOF is of the same order of magnitude found at the same overpotential for FeCo (oxy)hydroxides.^[4b]

STM images (Figure 2d) reveal that a slightly different surface morphology develops after ten OER cycles in comparison with the cathodic branch. The island type indicated as (i) is identical in terms of height and morphology to the cobalt oxide islands encountered after HER, that is, indicative of epitaxial O–Co–O/Au(111). Once

more, the individual island size changes towards larger patches of oxide film starting from 25–50 nm in diameter (see Figure SI.4) to 50–100 nm (see the overview image in Figure SI.6) after OER. In addition to the oxide, we observe another characteristic island type with a distinct smooth contrast (*ii*), and single atom deep pits in the Au surface (*iii*). Based on the apparent height (≈ 2.3 Å) extracted from line profiles (Figure SI.6), we can assign them to Au adatom islands, whereas the single atom deep pits (*iii*) reflect a missing layer of Au atoms. We attribute the emergence of these pits and islands to surface roughening and mobility of Au during the electrochemical cycles, as observed before in acidic solution.^[16] However, we note that in the reference experiment without the oxide we observe no similar changes to the Au(111) surface in the same potential window and electrolyte (Figure SI.6), indicating that the oxide is affecting Au adatom mobility.

The apparent oxide coverage in STM decreases from approximately 29% on the pristine Co–O synthesis to 14% after OER, implying a loss of cobalt to the electrolyte in the high potential region during oxidation and reduction of the Au(111). In the cyclic voltammograms, stable curves are observed from 2nd to 10th cycle (Figure SI.7) whereas changes are observed between the first and second voltage sweep. This behavior is consistent with a loss of cobalt oxide dissolved in the electrolyte occurring in the initial reorganization process of the $\text{CoO}_x/\text{Au}(111)$ interface, after which the system appears to stabilize. The ability of the Au substrate to support the stability of an atomically thin cobalt oxide during electrochemistry is underlined by the transformation of an initial minority island type (less than 10%) comprising a double bilayer, that is, two layers of $\text{Co–O}^{[13b]}$ on the freshly prepared samples (Figure SI.4). Interestingly, the resulting morphology after the electrochemical experiments only contain the single-layer oxide, which emphasizes a substantial reorganization of the oxide under electrochemical environment, and implies therefore that the active oxide morphology is largely determined by the exposure to electrochemical conditions rather than the initially prepared island structure.

To understand the fundamental nature of the transitions occurring during formation of the active oxide interface observed in Figure 2, we used STM and XPS to systematically monitor the response of the system to varying chemical environments, reflected by the conditions of pure vapor ($\text{H}_2\text{O}(g)$), and those in liquid ($\text{H}_2\text{O}(l)$). The STM image in Figure 3a reflects a fresh Co–O bilayer sample from Figure 1 after immersion under a liquid water droplet at room temperature, imaged in vacuum after the exposure. After this treatment the apparent coverage and distribution of islands on the surface is unchanged relative to the pristine sample, but the O content increases by a factor of 1.72, as measured with XPS (Figure 3d,e). This is attributed to the formation of O–Co–O trilayers on Au(111), which has an expected ratio of ≈ 1.8 compared to Co–O for the given XPS surface sensitivity.^[17] Further, probing the effect of oxygen free H_2O vapor ($\text{H}_2\text{O}(g)$) (300 K, 10 mbar) on the pristine Co–O sample, we again observe an unchanged island size

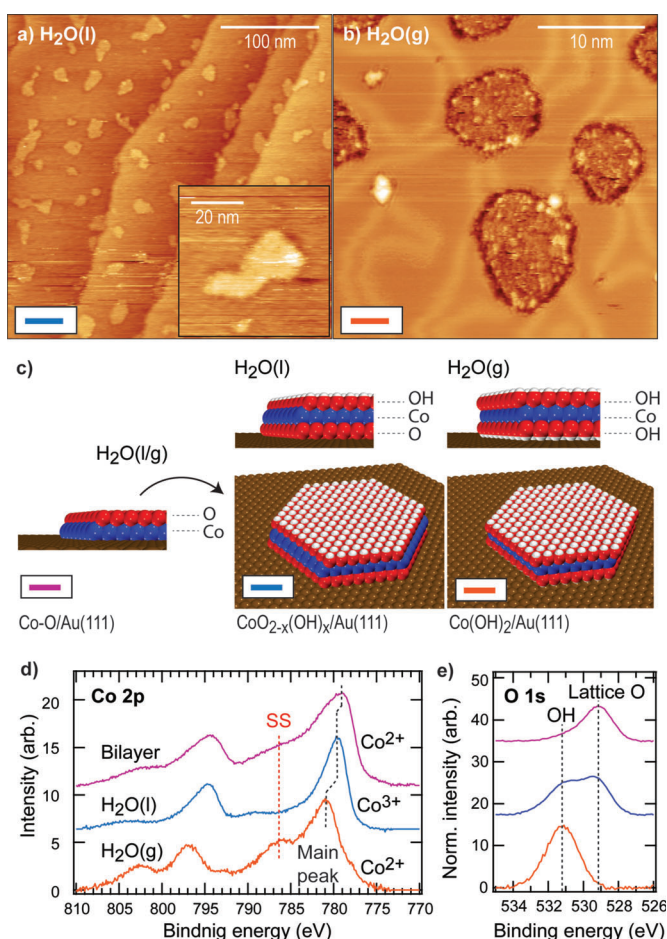


Figure 3. STM images of $\text{CoO}_{2-x}(\text{OH})_x$ nanoislands on Au(111). a) $\text{CoO}(\text{OH})$ trilayers after immersion into liquid H_2O . b) $\text{Co}(\text{OH})_2$ trilayers derived from bilayer exposed to 10 mbar H_2O vapor at room temperature. c) Ball models of $\text{CoO}(\text{OH})$ and $\text{Co}(\text{OH})_2$, respectively. d) XPS Co 2p region. SS indicates shakeup satellites distinct for Co^{2+} . e) O 1s spectra corresponding to the samples shown in (d). STM parameters: (a) -1.06 V/ -0.31 nA (both overview image and inset) and (b) -1.51 V/ -0.29 nA.

(Figure 3b) and an increase in relative XPS O1s area of 1.76, which is similarly matching O–Co–O trilayers.

In both of these cases, the transitions occur through a facile incorporation of O without apparent redistribution or agglomeration of individual islands. However, from the deconvolution of the O 1s spectrum into lattice oxygen and OH components in Figure 3e^[18] we detect a marked difference in the level of hydroxylation, which is much higher than the partial hydroxylation obtained at saturation for the trilayer in H_2O gas in the vacuum pressure regime (previously assigned to $\text{CoO}_{1.67}\text{OH}_{0.33}$).^[15] Whereas the ratio of the O and OH components approaches 1:1 in Figure 3e for the water droplet, the O1s peak is surprisingly shifted completely to the OH position in water vapor, reflecting that the structure is fully hydroxylated. In the corresponding ball models (Figure 3c) we propose the hydroxyl species after exposure to liquid water first to be situated in the top oxygen layer leading to a $\text{CoO}(\text{OH})$ structure, whereas for the $\text{Co}(\text{OH})_2$ formed in water vapor, the H also occupies positions on the lower

oxygen layer. In agreement, the corresponding XPS Co 2p spectra (Figure 3d) reveal that the initial high spin Co^{2+} state in the bilayer shifts to higher binding energy by ≈ 0.5 eV after exposure to liquid water, evidencing a change towards pure Co^{3+} ,^[13b] the spectrum being almost identical to bulk CoOOH .^[19] For the $\text{Co}(\text{OH})_2$ trilayer, the spectrum compares well to bulk $\text{Co}(\text{OH})_2$ compounds,^[19] confirming the structural model depicted in Figure 3c, with cobalt in the 2+ oxidation state.

The STM and XPS results clearly show that the cobalt oxide can adopt a generalized $\text{CoO}_{2-x}(\text{OH})_x$ trilayer structure on the Au(111) surface, where the x reflects a flexible degree of hydroxylation depending on conditions. Comparing the STM characteristics of the $\text{CoO}_{2-x}(\text{OH})_x$ phase and the cobalt oxide islands after electrochemical cycling in our experiments, we observe that the phases are qualitatively the same. The absence of a moiré pattern on the basal plane of the oxide islands in STM images of the $\text{CoO}_{2-x}(\text{OH})_x$ trilayers in all cases points to the pseudomorphic growth reported for $\text{CoOOH}_{0.33}$.^[15] This general feature of the trilayers, as opposed to the expanded growth of Co–O bilayer, can be rationalized in terms of different polarity compensation mechanisms that can increase the film stability (see further details in the supplementary discussion 1.2).

The pronounced agglomeration of the cobalt oxide observed after CV in alkaline conditions, which is not seen in pure water, can be attributed uniquely to the influence of the 0.1M NaOH electrolyte, since we observe a comparable degree of agglomeration in STM images of a reference sample immersed in the electrolyte solution at an open circuit potential (OCP) of -0.35 V (Figure SI.8). At this potential and pH value (13), the $\text{Co}(\text{OH})_2$ phase is expected according to the Pourbaix diagram for the cobalt- H_2O system,^[7d,24] indicating that transformation from Co–O bilayer to $\text{Co}(\text{OH})_2$ trilayer is likely to take place. Such a transition might explain an accompanying agglomeration into the observed larger thin-film islands with shapes that are, however, much less regular than those observed after CV. This implies that under an applied potential further reshaping into a crystalline well-defined hexagonal $\text{CoO}_{2-x}(\text{OH})_x$ morphology with sharp low-index edges takes place. Adding to the explanation behind this difference, we also note that potentials that drive HER are also sufficiently negative to intermittently reduce the CoO_x islands to metallic Co. This is in accord with Pourbaix diagrams of Co and also with the redox couple observed around -1 V in the CV shown in the supporting information (Figure SI.5).

From an electrocatalytic point of view, the key finding is that the catalytically enhanced cobalt oxide/Au interface can exploit facile transitions between $\text{CoO}_{2-x}(\text{OH})_x$ phases reported in studies accessing the state of cobalt oxide during electrochemical OER operation, for example, CoO_2 , CoOOH oxyhydroxide, and $\text{Co}(\text{OH})_2$.^[9a,25] The wetting effect of gold means that such transformations occur directly without passing through the structurally very different spinel-type Co_3O_4 phase, which features as the predominant, but inactive intermediate bulk phase at low positive potentials in the Pourbaix stability diagram of Co oxides in alkaline solutions.^[7d,9a,10] We thus propose that the Au acts in

a beneficial way to significantly stabilize the active $\text{CoO}(\text{OH})$ -like phase in a wider region of potentials and reduces the switching potential at which the most active phase is formed. For the gold supported cobalt oxides, this translates into a significant lowering of the apparent overpotential in the OER compared with bulk materials. The results fully explain that OER activity enhancement on gold supported cobalt oxide is strongest in the limit below one ML oxide and that the effect is observed to diminish when the oxide film is too thick, confirming the picture of an active stabilizing effect of a thin oxide on gold.^[5a] In fact, the 0.30 V overpotential measured for OER here is in precise agreement with the theoretically predicted overpotential of 0.33 V for O-Co-O islands on Au(111).^[13a] The same study also pointed to a much higher catalytic activity of edge sites, and a promising route to further rational optimization of the catalytic OER activity may therefore be concentrated on stabilizing initial high edge-exposure morphologies by reducing the agglomeration effect due to the electrolyte.

Acknowledgements

The Aarhus group acknowledges the Aarhus University Center for Integrated Materials Research (iMAT) and financial support from Lundbeckfonden and Villum Fonden. Z.S. would like to acknowledge financial support from the Chinese Scholarship Council (CSC). D.G. acknowledges PICT 2014 -1415. We acknowledge fruitful discussions with Alex Walton, University of Manchester.

Conflict of interest

The authors declare no conflict of interest.

Keywords: electrocatalysis · metal oxides · oxygen evolution reactions · scanning tunneling microscopy

- [1] C. C. McCrory, S. Jung, I. M. Ferrer, S. M. Chatman, J. C. Peters, T. F. Jaramillo, *J. Am. Chem. Soc.* **2015**, *137*, 4347–4357.
- [2] a) Y. Sun, S. Gao, F. Lei, J. Liu, L. Liang, Y. Xie, *Chem. Sci.* **2014**, *5*, 3976–3982; b) X. Deng, H. Tüysüz, *ACS Catal.* **2014**, *4*, 3701–3714; c) L. Liao, Q. Zhang, Z. Su, Z. Zhao, Y. Wang, Y. Li, X. Lu, D. Wei, G. Feng, Q. Yu, *Nat. Nanotechnol.* **2014**, *9*, 69–73; d) F. Jiao, H. Frei, *Energy Environ. Sci.* **2010**, *3*, 1018–1027; e) M. E. Lyons, M. P. Brandon, *J. Electroanal. Chem.* **2010**, *641*, 119–130.
- [3] a) M. Grzelczak, J. Zhang, J. Pfrommer, J. Hartmann, M. Driess, M. Antonietti, X. Wang, *ACS Catal.* **2013**, *3*, 383–388; b) J. Rosen, G. S. Hutchings, F. Jiao, *J. Am. Chem. Soc.* **2013**, *135*, 4516–4521.
- [4] a) G. Wu, N. Li, D.-R. Zhou, K. Mitsuo, B.-Q. Xu, *J. Solid State Chem.* **2004**, *177*, 3682–3692; b) M. S. Burke, M. G. Kast, L. Trotochaud, A. M. Smith, S. W. Boettcher, *J. Am. Chem. Soc.* **2015**, *137*, 3638–3648; c) M. S. Burke, L. J. Enman, A. S. Batchellor, S. Zou, S. W. Boettcher, *Chem. Mater.* **2015**, *27*, 7549–7558.

- [5] a) B. S. Yeo, A. T. Bell, *J. Am. Chem. Soc.* **2011**, *133*, 5587–5593; b) X. Lu, Y. H. Ng, C. Zhao, *ChemSusChem* **2014**, *7*, 82–86; c) B. Y. Kim, I.-B. Shim, Z. O. Araci, S. S. Saavedra, O. L. Monti, N. R. Armstrong, R. Sahoo, D. N. Srivastava, J. Pyun, *J. Am. Chem. Soc.* **2010**, *132*, 3234–3235; d) R. Frydendal, M. Busch, N. B. Halck, E. A. Paoli, P. Krttil, I. Chorkendorff, J. Rossmeisl, *ChemCatChem* **2015**, *7*, 149–154; e) A. L. Strickler, M. Escudero-Escribano, T. F. Jaramillo, *Nano Lett.* **2017**, *17*, 6040–6046.
- [6] D. Gao, Y. Zhang, Z. Zhou, F. Cai, X. Zhao, W. Huang, Y. Li, J. Zhu, P. Liu, F. Yang, G. Wang, X. Bao, *J. Am. Chem. Soc.* **2017**, *139*, 5652–5655.
- [7] a) X. Li, P. E. Siegbahn, *J. Am. Chem. Soc.* **2013**, *135*, 13804–13813; b) M. García-Mota, M. Bajdich, V. Viswanathan, A. Vojvodic, A. T. Bell, J. K. Nørskov, *J. Phys. Chem. C* **2012**, *116*, 21077–21082; c) G. Mattioli, P. Giannozzi, A. Amore Bonapasta, L. Guidoni, *J. Am. Chem. Soc.* **2013**, *135*, 15353–15363; d) M. Bajdich, M. García-Mota, A. Vojvodic, J. K. Nørskov, A. T. Bell, *J. Am. Chem. Soc.* **2013**, *135*, 13521–13530.
- [8] a) D. Friebel, M. Bajdich, B. S. Yeo, M. W. Louie, D. J. Miller, H. S. Casalongue, F. Mbuga, T.-C. Weng, D. Nordlund, D. Sokaras, *Phys. Chem. Chem. Phys.* **2013**, *15*, 17460–17467; b) M. Zhang, M. De Respinis, H. Frei, *Nat. Chem.* **2014**, *6*, 362–367; c) A. Bergmann, E. Martínez-Moreno, D. Teschner, P. Chernev, M. Gliech, J. F. De Araújo, T. Reier, H. Dau, P. Strasser, *Nat. Commun.* **2015**, *6*, 8625; d) J. G. McAlpin, Y. Surendranath, M. Dinca, T. A. Stich, S. A. Stoian, W. H. Casey, D. G. Nocera, R. D. Britt, *J. Am. Chem. Soc.* **2010**, *132*, 6882–6883; e) M. Risch, F. Ringleb, M. Kohlhoff, P. Bogdanoff, P. Chernev, I. Zaharieva, H. Dau, *Energy Environ. Sci.* **2015**, *8*, 661–674; f) P. Du, O. Kokhan, K. W. Chapman, P. J. Chupas, D. M. Tiede, *J. Am. Chem. Soc.* **2012**, *134*, 11096–11099.
- [9] a) M. Favaro, J. Yang, S. Nappini, E. Magnano, F. M. Toma, E. J. Crumlin, J. Yano, I. D. Sharp, *J. Am. Chem. Soc.* **2017**, *139*, 8960; b) F. Reikowski, F. Maroun, N. Di, P. Allongue, M. Ruge, J. Stettner, O. M. Magnussen, *Electrochim. Acta* **2016**, *197*, 273–281.
- [10] a) E. Fabbri, M. Nachttegaal, T. Binninger, X. Cheng, B.-J. Kim, J. Durst, F. Bozza, T. Graule, R. Schäublin, L. Wiles, *Nat. Mater.* **2017**, *16*, 925–931; b) J. Yang, J. K. Cooper, F. M. Toma, K. A. Walczak, M. Favaro, J. W. Beeman, L. H. Hess, C. Wang, C. Zhu, S. Gul, *Nat. Mater.* **2017**, *16*, 335–341.
- [11] a) H. Dau, C. Limberg, T. Reier, M. Risch, S. Roggan, P. Strasser, *ChemCatChem* **2010**, *2*, 724–761; b) A. Grimaud, O. Diaz-Morales, B. Han, W. T. Hong, Y.-L. Lee, L. Giordano, K. A. Stoerzinger, M. T. Koper, Y. Shao-Horn, *Nat. Chem.* **2017**, *9*, 457; c) J. Huang, J. Chen, T. Yao, J. He, S. Jiang, Z. Sun, Q. Liu, W. Cheng, F. Hu, Y. Jiang, Z. Pan, S. Wei, *Angew. Chem. Int. Ed.* **2015**, *54*, 8722–8727; *Angew. Chem.* **2015**, *127*, 8846–8851; d) K. A. Stoerzinger, O. Diaz-Morales, M. Kolb, R. R. Rao, R. Frydendal, L. Qiao, X. R. Wang, N. B. Halck, J. Rossmeisl, H. A. Hansen, *ACS Energy Lett.* **2017**, *2*, 876–881; e) F. Song, X. Hu, *Nat. Commun.* **2014**, *5*, 4477.
- [12] a) B. Wurster, D. Grumelli, D. Hötger, R. Gutzler, K. Kern, *J. Am. Chem. Soc.* **2016**, *138*, 3623–3626; b) D. Grumelli, B. Wurster, S. Stepanow, K. Kern, *Nat. Commun.* **2013**, *4*, 2904.
- [13] a) J. Fester, M. García-Melchor, A. Walton, M. Bajdich, Z. Li, L. Lammich, A. Vojvodic, J. Lauritsen, *Nat. Commun.* **2017**, *8*, 14169; b) A. S. Walton, J. Fester, M. Bajdich, M. A. Arman, J. Osiecki, J. Knudsen, A. Vojvodic, J. V. Lauritsen, *ACS Nano* **2015**, *9*, 2445–2453.
- [14] R. Subbaraman, D. Tripkovic, K.-C. Chang, D. Strmcnik, A. P. Paulikas, P. Hirunsit, M. Chan, J. Greeley, V. Stamenkovic, N. M. Markovic, *Nat. Mater.* **2012**, *11*, 550.
- [15] J. Fester, A. Walton, Z. Li, J. V. Lauritsen, *Phys. Chem. Chem. Phys.* **2017**, *19*, 2425–2433.
- [16] a) D. J. Trevor, C. E. Chidsey, D. N. Loiacono, *Phys. Rev. Lett.* **1989**, *62*, 929; b) H. Honbo, S. Sugawara, K. Itaya, *Anal. Chem.* **1990**, *62*, 2424–2429.
- [17] J. Fester, Z. Sun, J. Rodríguez-Fernández, A. Walton, J. V. Lauritsen, *J. Phys. Chem. B* **2017**, *121*, 261–271.
- [18] M. A. Henderson, *Surf. Sci. Rep.* **2002**, *46*, 1–308.
- [19] a) M. C. Biesinger, B. P. Payne, A. P. Grosvenor, L. W. Lau, A. R. Gerson, R. S. C. Smart, *Appl. Surf. Sci.* **2011**, *257*, 2717–2730; b) J. Yang, H. Liu, W. N. Martens, R. L. Frost, *J. Phys. Chem. C* **2010**, *114*, 111–119.
- [20] P. Tasker, *J. Phys. C* **1979**, *12*, 4977.
- [21] J. Fester, M. Bajdich, A. S. Walton, Z. Sun, P. N. Plessow, A. Vojvodic, J. V. Lauritsen, *Top. Catal.* **2016**, *1*–10.
- [22] a) M. De Santis, A. Buchsbaum, P. Varga, M. Schmid, *Phys. Rev. B* **2011**, *84*, 125430; b) W. Weiss, W. Ranke, *Prog. Surf. Sci.* **2002**, *70*, 1–151; c) X. Deng, K. Yao, K. Sun, W.-X. Li, J. Lee, C. Matranga, *J. Phys. Chem. C* **2013**, *117*, 11211–11218.
- [23] a) C. Noguera, J. Goniakowski, *Chem. Rev.* **2013**, *113*, 4073–4105; b) D. Cappus, C. Xu, D. Ehrlich, B. Dillmann, C. Ventrice, Jr., K. Al Shamery, H. Kuhlenbeck, H.-J. Freund, *Chem. Phys.* **1993**, *177*, 533–546.
- [24] E. Garcia, J. Santos, E. Pereira, M. Freitas, *J. Power Sources* **2008**, *185*, 549–553.
- [25] J. A. Koza, Z. He, A. S. Miller, J. A. Switzer, *Chem. Mater.* **2012**, *24*, 3567–3573.

Manuscript received: April 16, 2018

Revised manuscript received: June 16, 2018





Accepted manuscript online: July 7, 2018

Version of record online: ■■■■■■

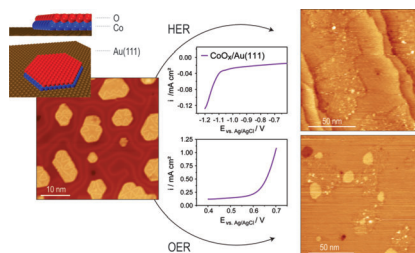
Communications



Oxygen Evolution Reaction

J. Fester, A. Makoveev, D. Grumelli,
R. Gutzler, Z. Sun,
J. Rodríguez-Fernández, K. Kern,
J. V. Lauritsen*    

The Structure of the Cobalt Oxide/Au
Catalyst Interface in Electrochemical
Water Splitting



One half-reaction of electrochemical water splitting is the oxygen evolution reaction, which is promoted by the catalytic synergy between cobalt oxide and gold. The mechanism behind that enhancement effect is still not understood. It is revealed that the supporting gold substrate uniquely favors a flexible cobalt-oxyhydroxide/Au interface in the electrochemically active potential window and thus suppresses the formation of less active bulk cobalt oxide morphologies.